Joint Special Interest Group meeting between euspen and ASPE
Advancing Precision in Additive Manufacturing
TU Berlin, Germany, October 2025
www.euspen.eu

Understanding next-layer effects of defects in laser powder bed fusion of nickel superalloy 625

Jesse Redford[1], Jason Fox[1], Chris Evans[1,2], Brigid Mullany[2]

[1]*National Institute of Standards and Technology (NIST), Gaithersburg, MD, USA*

[2]*University of North Carolina at Charlotte, Charlotte, NC, USA*

Jesse.redford@nist.gov

Abstract

In-situ monitoring in laser powder bed fusion (PBF-LB) enables detection of process-induced defects during fabrication, offering opportunities for corrective action or early build termination. However, the layer-wise remelting characteristic of PBF-LB can modify or eliminate defects, meaning that an initial "true positive" detection may not persist in subsequent layers. This study examines the evolution of seeded defects across layers to better understand these next-layer "self-healing" effects. Twelve nickel superalloy 625 (IN625) specimens containing three defect types (open-hole, lack of fusion, and keyhole) were fabricated with controlled process parameters. Cross-sectional metallography was used to quantify changes in melt pool morphology and surface topography above defect regions. Initial results for open-hole defects are presented, highlighting defect persistence and transformation mechanisms.

additive manufacturing, laser powder bed fusion, defect evolution, self-healing

1. Introduction

Defect formation remains a primary barrier to the widespread adoption of metal laser powder bed fusion (PBF-LB/M) in critical applications. While advances in process monitoring and non-destructive evaluation (NDE) have improved detection capabilities, interpreting these signals is complicated by the dynamic and violent nature of the process. In particular, the repeated layer deposition and partial remelting inherent to PBF-LB/M can alter or even eliminate previously formed defects, a phenomenon often referred to as "self-healing". Understanding how such mechanisms propagate from layer to layer can aid in the development of measurement strategies, probability of detection models, and quality assurance initiatives. This study investigates how seeded defects influence melt pool geometry and surface topography in overlying layers, extending prior studies covered in [1-4]. Twelve nickel superalloy 625 (IN625) specimens with controlled defect types were fabricated under defined process conditions. Section 2 outlines the design, parameters, and metallographic procedures. Section 3 presents micrographs for 0–4 layers deposited over a nominal 1.00 mm and 0.350 mm open-hole defect, with initial observations and future work to be included in the poster summarized in Section 4.

2. Methodology

Twelve defect-bearing specimens were fabricated with an EOS M290 commercial additive manufacturing (AM) system. Each specimen contained six rectangular "logs" (4 mm × 20 mm × 10.8 mm in the x, y, and z directions) labeled A, B, C, D, E, or F, each seeded with five defects: open-hole (OH, 0.35 mm and 1.00 mm diameter), lack of fusion (LOF, 2.5 mm length), and keyhole (KH, 0.25 mm and 0.75 mm diameter). For specimens 1, 4, 5, 8, 9, and 10, logs B–E were overbuilt with 1–4 layers above the defect location; for specimens 2, 3, 6, 7, and 11, the overbuild comprised 5, 8, 11, or 15 layers. Logs A and F, located at each end, had zero overbuild layers in all specimens. A coordinate line was fused to the top surface to provide a fiducial for multi-modal data registration. While measurements for all specimens are ongoing, the present analysis focuses on specimen 8. Figure 1 provides a schematic overview of the seeded defect geometries and build configuration.

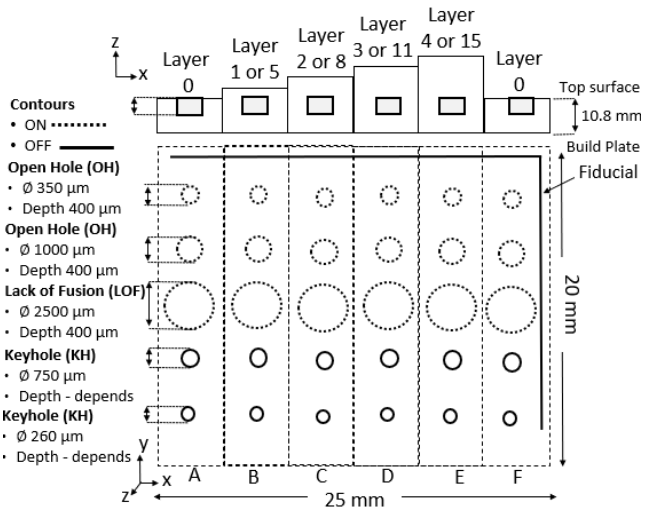

Figure 1. Example of artifact geometry with seeded defect types, size, and locations.

Table 1 lists the build parameters used for manufacturing the defect samples. The seeded keyhole (KH) and lack of fusion (LOF) defects were generated by adjusting the power and laser velocity parameters within the designed areas shown in Figure 2. In addition to the power and velocity adjustments, the hatch spacing was also increased to 220 µm in the LOF regions.

The open-hole (OH) defects were created geometrically within the part design. Down skin parameters were turned off to simulate the conditions of building over an unintentionally created defect. The bulk and contour parameters in Table 1 reflect vendor-recommended settings for the IN625 alloy. This also includes a 40 µm programmed layer thickness, hatch spacing of 110 µm, 67° layer-wise rotations, stripe width of 10 mm, and build plate temperature of 80 °C. Argon is used as the shielding gas flowing from the back to the front of the machine. The volumetric energy density (VED) for each category in Table 1 is calculated as VED = $\frac{P}{v \cdot h \cdot l}$, where P is the laser power, v is scan speed, h is the hatch spacing, and l is the programmed layer thickness.

Table 1 Summary of process parameters used to manufacture samples.

Category	Contour	Power (watts)	Velocity (mm/s)	Volumetric Energy Density (J/mm³)
Bulk Build	Yes	285	960	69
Contour (Pass 1)	n/a	138	300	104
Contour (Pass 2)	n/a	80	800	22
Open-hole (OH)	Yes	285	960	69
Keyhole (KH)	No	285	200	323
Lack-of-fusion (LOF)	Yes	285	1920	16

Initial inspection of sample 8 included bright field (BF) micrographs, scanning electron microscope (SEM), and electron backscatter-diffraction (EBSD) measurements after being sectioned along a given defect row, with top and bottom halves, T and B, representing the two faces of the cross-sectioned sample. For each defect type, the two halves are separated by one kerf of the width of the electrical discharge machining (EDM) wire plus the reduction in thickness due to polishing and/or etching. A schematic of one-half of the sectioned sample geometry after wire-EDM is shown in Figure 2. The typical polishing operation reduces the thickness of the sample by 100 µm to 300 µm, which is large relative to the seeded defects. Preliminary EBSD analysis was performed on the cross-section of S8-OH-0.35mm-B to inspect the effect on microstructure characteristics when building on top of a large pore. The notation S8-OH-0.35mm-B is used as naming convention to represents the sample number, defect type, defect diameter, and bottom (B) or top half (T). Next, the sample was etched and stitched brightfield images of the entire cross-section of each sample were collected using an optical microscope (Zeiss AxioImager.Z2) with a 5× objective (3.45 µm per pixel) and native ZenCore3.2 software. Post-processing and analysis of the micrographs were performed using ImageJ to characterize defect dimensions and melt pool structure above and below-embedded defects. Average melt pool areas and depths corresponding to the different scan parameters were tabulated in addition to pore locations, sizes, and frequency.

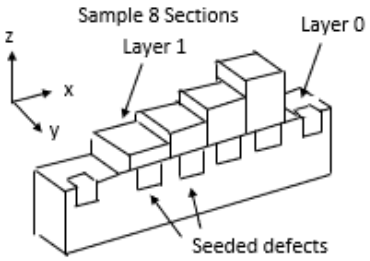

Figure 2. Schematic of the cross-sections of sample 8 after wire EDM.

3. Results

3.1. Example of Large & Small Open-Hole Defect

For 1.00 mm open-hole defects in Figure 3, surface depressions decreased from ≈ 250 µm (layer 1) to ≈ 60 µm (layer 4). The measurements process across each defect type involved visually fitting a line to the topmost surface, then determining the vertical distance to the deepest valley within the center-region of the defect area. Pore accumulation was observed around contour pass boundaries.

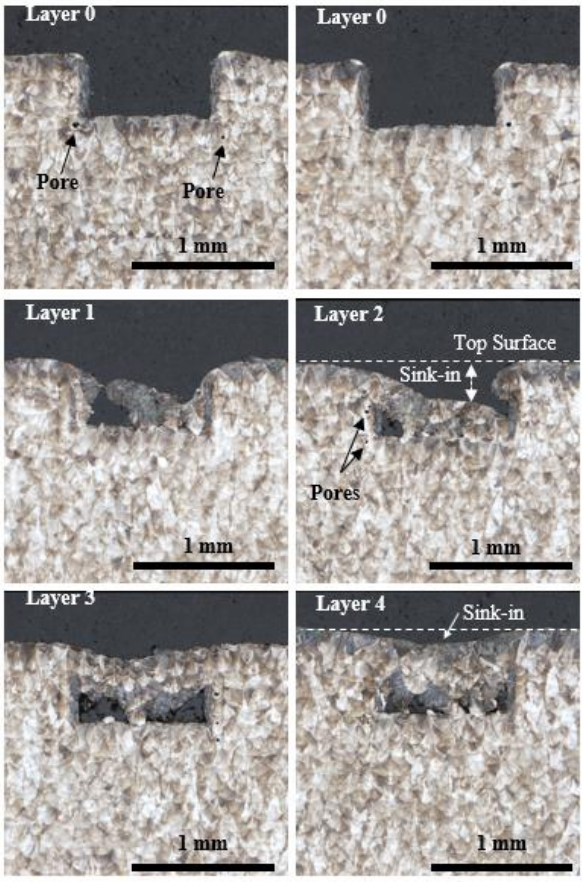

Figure 3. Bright-field micrographs of 1.0 mm open hole defect with zero and multiple layers built on top.

Micrographs of the smaller 0.35 mm open-hole defect (S8-OH-0.35-B) in Figure 4 did not show signs of significant collapse of material. Small depressions of 80 µm, 40 µm, 30 µm, and 12 µm were recorded for layers 1, 2, 3, and 4, respectively. Melt pool depths remained largely unchanged over defect regions, suggesting that top-surface depressions are primarily due to powder consolidation rather than melt pool instability. Accumulations of pores are observed around the seeded defect, similar to the 1.00 mm OH defects shown in Figure 3.

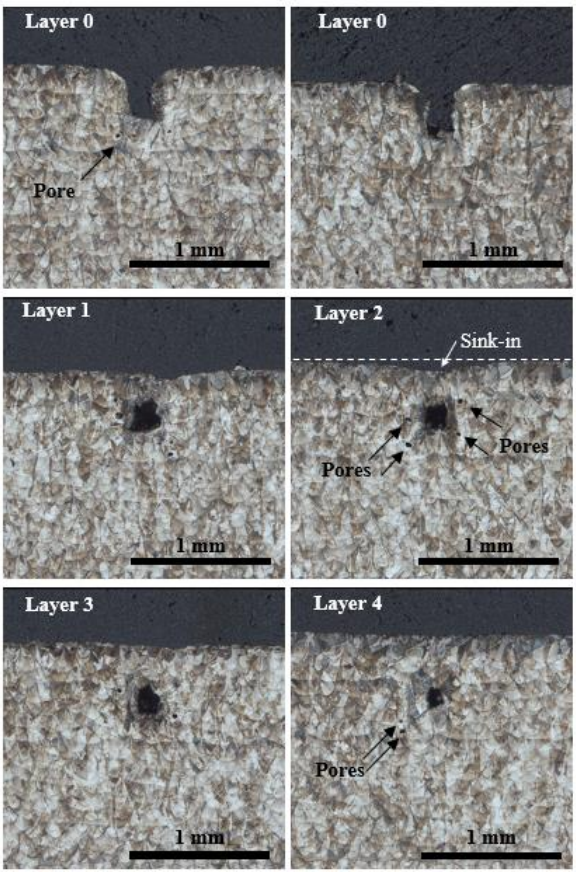

Figure 4. Bright field micrographs of 0.35 mm open hole defect with zero and multiple layers built on top.

Figure 5 illustrates a conceptual model of the depression along the nominal top surface as a function of the number of layers built on top of a defect. Melt pool depth measurements of the first layer built over the defect region remain mostly constant despite building on top of multiple layers of powder; this suggests the sink-in is not due to a reduction/change in melt pool geometry. Instead, powder consolidation is assumed to be the dominant mechanism creating the top surface depression.

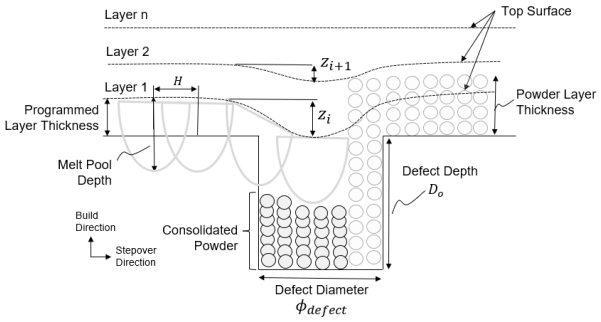

Figure 5. Conceptual illustration of observed melt pool behavior and consolidation of powder within defect region. The sink-in along the top surface is a function of the initial defect size and the number of layers built on top.

4. Conclusions

Quantifying the detailed evolution of subsequent layers built on top of defects provides valuable insight into the self-healing process inherit to AM. A set of initial X ray computed tomography (XCT) measurements of select samples used in the study suggested an accumulation of pores near the seeded defects, therefore based only on this information it could have been incorrectly assumed that building over the seeded defects contributed to the development of these pores. However, with further investigation, micrographs clearly revealed that this accumulation of smaller pores was localized to the melt pools created by the first of two contour passes, which had a volumetric energy density 40 % larger that bulk build parameters (see Table 1), causing the melt pool to enter a keyhole mode. A top surface depression was evident up to the fourth layer over the 1.00 mm open-hole defect, however little to no discernible depressions were present in the fourth layer built over the smaller 0.35 mm open-hole defect. A simple model for predicting the evolution of the top surface depression as a function of the number of layers and original size of the defect will be reported in future work and included in the poster. Additional EBSD analysis of the samples will also be provided to highlight how local crystallographic texture in subsequent layers is affected when building on top of different defect types.

NIST Disclaimer

References

[1] Reese Z C, Fox J C, Kim F H, Taylor J and Evans C 2018 Effect of subsurface defects on the surface topography of additive manufactured components *ASPE 2018 Summer Topical Meeting: Advancing Precision in Additive Manufacturing*

[2] Fox J C, Allen A, Mullany B, Morse E, Isaacs R A, Lata M, Brackman P, Sood A, Allen A and Evans C 2021 Surface topography process signatures in nickel superalloy 625 additive manufacturing *Proc. 2021 SIG Additive Manufacturing: Advancing Precision in Additive Manufacturing*, Online

[3] Fox J, Evans C, Sood A, Isaacs R, Mullany B, Allen A and Morse E 2022 Weld track distortion in laser powder bed fusion of nickel superalloy 625 *Proc. ASPE–euspen Special Interest Group Meeting: Advancing Precision in AM*, Knoxville, TN, USA

[4] Fox J C, Sood A, Isaacs R, Brackman P, Mullany B, Morse E, Allen A, Costa Santos E and Evans C 2022 Surface feature characteristics of laser powder bed fusion of nickel superalloy 625 bulk regions *Procedia CIRP* **108** 531–536